coatings

MDPI

Article

Quality and Lifetime of Thin Parylene F-VT4 Coatings for Hermetic Encapsulation of Implantable Medical Devices

Esmaeil Afshari [1,2,*], Rik Verplancke [1,2], Maarten Cauwe [1,2] and Maaike Op de Beeck [1,2,*]

[1] Centre for Microsystems Technology (CMST), Technologiepark-Zwijnaarde 126, 9052 Ghent, Belgium; maarten.cauwe@imec.be (M.C.)
[2] Imec, Kapeldreef 75, 3001 Leuven, Belgium
* Correspondence: esmaeil.afshari@imec.be (E.A.); maaike.opdebeeck@imec.be (M.O.d.B.)

Abstract: This study comprehensively examines the barrier properties, aging behavior, and failure mechanisms of Parylene F-VT4 films, applied at four distinct thicknesses (0.3 µm, 0.6 µm, 0.9 µm, and 1.2 µm), as encapsulation layers for implantable medical devices. Parylene F-VT4, a fluorinated polymer known for its mechanical flexibility, thermal stability, and chemical inertness, is a promising candidate for long-term hermetic encapsulation. Parylene F-VT4 was uniformly deposited via a dedicated chemical vapor deposition (CVD) process typically used for Parylene depositions. The investigation of the Parylene F-VT4 films included pinhole density characterization, electrochemical impedance spectroscopy (EIS), and testing of coating lifetime based on the resistance of Cu meanders protected by Parylene F-VT4 when immersed in phosphate-buffered saline (PBS) under accelerated aging conditions (PBS at 60 °C) over 550 days. The EIS results demonstrated that thicker coatings (1.2 µm) exhibited excellent barrier properties and resistance to electrolyte penetration, whereas thinner coatings (0.3 µm and 0.6 µm) showed more rapid degradation due to microvoids and pinholes. The temporal evaluation of EIS spectra highlighted the gradual decrease in impedance magnitude, indicating the ingress of ions and water into the coating. The lifetime in PBS at 60 °C was determined by resistance-based lifetime measurements on Cu meander structures coated with Parylene F-VT4 coatings. The lifetime at 37 °C was calculated, assuming an acceleration factor of 2 per 10 °C increase in temperature, yielding lifetimes of approximately 25 days, 6.4 months, 2.3 years, and 4.5 years for 0.3 µm, 0.6 µm, 0.9 µm, and 1.2 µm coatings, respectively. These findings highlight the critical relationship between thickness and durability, providing valuable insights into the long-term performance of thin Parylene F-VT4 films for implantable devices.

Keywords: Parylene F-VT4; EIS; lifetime; implantable medical devices; biocompatible encapsulation

Academic Editors: Patrique Fiedler and José Carlos Fonseca

Received: 22 April 2025
Revised: 23 May 2025
Accepted: 26 May 2025
Published: 28 May 2025

Citation: Afshari, E.; Verplancke, R.; Cauwe, M.; Op de Beeck, M. Quality and Lifetime of Thin Parylene F-VT4 Coatings for Hermetic Encapsulation of Implantable Medical Devices. *Coatings* **2025**, *15*, 648. https://doi.org/10.3390/coatings15060648

1. Introduction

Implantable medical devices have revolutionized healthcare, providing critical solutions for patient diagnosis, treatment, and monitoring in various therapeutic areas, from cardiology to neurology [1–3]. As the technology behind these devices advances, the need for biocompatible, hermetic, and flexible encapsulation becomes increasingly critical [4]. These encapsulation layers protect the sensitive electronic components of the device against harsh physiological environments, and they also safeguard surrounding tissue from potential adverse effects and non-biocompatible materials [5,6].

Traditional rigid materials such as glass, titanium, and Ti alloys have been used widely as device protection, but they present limitations in terms of device miniaturization and

flexibility [7]. These limitations led to the growing interest in biocompatible polymeric materials, such as Parylene, which is known for its unique combination of desirable properties. Parylene (poly-para-xylylene (PPX)) has emerged as a promising material for biomedical encapsulation due to its flexibility, chemical inertness, low relative permittivity, elevated breakdown voltage, and exceptional barrier properties [8–10]. Parylene films are deposited through a dedicated chemical vapor deposition (CVD) polymerization process that precisely controls the vaporization and polymerization of Parylene dimer. This technique ensures the formation of ultra-thin coatings with precise thickness control and excellent conformality [11]. Furthermore, the deposition process takes place at room temperature and is solvent-free, making Parylene layers ideal for the coating of biomedical implants without damaging their sensitive components.

Among the different Parylene types, Parylene C, Parylene N, and Parylene F-VT4 are biocompatible. Parylene F-VT4 is especially noteworthy for its enhanced mechanical flexibility and improved thermal stability, due to its unique chemical structure incorporating fluorine atoms [12,13]. This thermal robustness makes it suitable for steam sterilization (autoclaving), during which exposure to high temperatures (121–134 °C) is needed without material degradation [14]. Additionally, its excellent thermal stability allows compatibility with atomic layer deposition (ALD) processes. By depositing inorganic ALD nanolayers on Parylene films, a composite multilayer encapsulation can be created, resulting in a significantly increased durability of the encapsulation due to the superior barrier properties of the Parylene/ALD multilayer [15].

While increasing the Parylene thickness will enhance hermeticity and hence extend the lifetime of an implanted device, it may also introduce challenges related to the performance of both electrode-based and mechanical sensors. For electrode-based sensors, a thick encapsulation layer can increase the distance between the recessed electrodes and the tissue being measured or stimulated, potentially causing signal distortion or attenuation [16]. For capacitive electrode sensors, the insulating Parylene layer covering the electrode will be part of the sensor, and sensitivity will thus obviously decrease with increasing Parylene thickness [17,18]. For implanted devices that rely on mechanical interaction with the surrounding medium, such as pressure sensors, actuators, and certain MEMS devices, increasing the thickness of the encapsulation will decrease sensor performance due to the additional stiffness and mass loading [19,20]. These issues can be mitigated by reducing the encapsulation thickness but at the cost of a lower hermeticity. Hence, a compromise has to be found between sensor functionality and required hermeticity for the envisaged lifetime of the implanted device.

This paper aims to investigate the performance and lifetime of thinner Parylene F-VT4 films in order to evaluate these films as potential flexible and hermetic encapsulation layers for implantable medical devices. To achieve this, dedicated test structures are fabricated, with Parylene F-VT4 protective films of various thicknesses, ranging from 0.3 µm to 1.2 µm. We conducted a series of pinhole tests, resistance-based lifetime assessment, and electrochemical impedance spectroscopy (EIS), all during long-term immersion of the test structures in phosphate-buffered saline (PBS). In order to use sensitive test structures, copper was selected as the underlying material since it will corrode very fast when exposed to moisture. EIS is an effective electrochemical technique utilized to assess coating properties and their evolution under corrosive environmental conditions [21–24]. For clarity, Parylene F-VT4 will be referred to as 'Parylene' throughout the rest of the paper.

2. Materials and Methods

2.1. Sample Preparation

Copper was selected as the underlying material for evaluating the barrier performance of Parylene, since copper is known to be highly susceptible to corrosion when exposed to physiological fluids, such as PBS [25]. Glass substrates (5 × 5 cm^2) were initially cleaned, followed by sputtering of 50 nm titanium–tungsten (TiW) and 1 µm copper using an Alcatel SCM600 system. TiW is used to enhance copper adhesion to glass. These plain copper-coated glass samples were used for pinhole density analysis after being covered with Parylene coatings, as described in the following section.

For electrochemical impedance spectroscopy (EIS) measurements and for resistance-based lifetime tests, the TiW/Cu sputtered layers were patterned using photolithography and wet etching. After dehydration of the samples at 120 °C for 10 min, photoresist (S1818) was spin-coated at 4000 rpm for 60 s, followed by a soft bake at 90 °C for 2 min. UV exposure (75 mJ/cm^2) was performed, and the resist was developed in Microposit developer (Micro Resist Technology GmbH, Berlin, Germany) for 30 s, followed by a post-bake at 120 °C for 30 min to improve resist adhesion and stability. Cu wet etching was done using Mecbrite CA92 (MEC Europe NV., Ghent, Belgium) for 20 s, followed by TiW etching in H_2O_2 at 55 °C for ~25 s. The pattern, illustrated in Figure 1a, included meanders of three different linewidths (30 µm, 40 µm, and 50 µm) with a total length of ~25 cm for each meander, which were used for resistance-based lifetime testing. A rectangular plane (~2 cm^2) adjacent to the meanders was used for the EIS measurements.

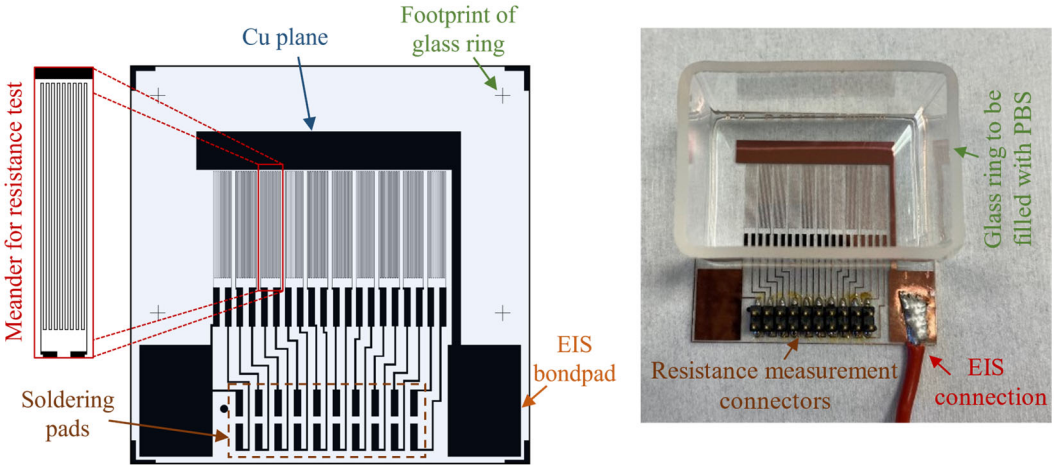

Figure 1. (**a**) Mask design used for photolithography and patterning of the sputtered layers. (**b**) Image of the patterned Cu sample with a glued ring on the glass to be filled with PBS.

On both types of test structures, Parylene was uniformly deposited by a dedicated chemical vapor deposition (CVD) process using a C30S Comelec tool, after applying an A-174 silane adhesion promoter. Four target coating thicknesses—0.3 µm, 0.6 µm, 0.9 µm, and 1.2 µm—were achieved by controlling the amount of Parylene dimer used during the deposition process. The resulting film thicknesses were verified on silicon dummy samples using a surface profiler (Alpha-Step IQ, KLA-Tencor Corp., Milpitas, CA, USA).

To enable immersion of the copper patterns in PBS while performing electrical tests, a local fluid container was realized by gluing a glass ring on the test substrate using silicone glue, as shown in Figure 1b. Connectors and wires were soldered to Cu bondpads next to the fluid container, in order to connect the Cu meanders to the resistance measurement system and the Cu plane to the EIS potentiostat. After soldering, silicone glue was applied on the soldered contact pads and wires to protect these structures from damage by water

drops and vapor during the test. This protection is very important since we envisaged long-term soaking tests at elevated temperature.

2.2. Pinhole Test

The pinhole test was employed to assess the defect density and pinhole uniformity of the Parylene layer at various tested thicknesses. This test provides crucial insights into the coating's ability to act as a continuous and defect-free encapsulation layer, as pinholes can lead to rapid failure of the encapsulation layer.

Unpatterned copper samples were coated with Parylene and immersed in a Cu etching solution (MecbriteCA92 (MEC Europe NV., Ghent, Belgium), a mixture of H_2SO_4, $CuSO_4$, H_2O_2, and surfactants by Mec Europe) at room temperature. If pinholes are present in the coating, the etching solution will reach the Cu fast through these defects, attacking the underlying Cu and resulting in the formation of vias at the pinhole sites. With longer etch time, the etchant causes undercutting of the copper around the pinholes, enlarging the vias and making them easily visible under an optical microscope [25,26]. To ensure clear visualization of the vias while minimizing the risk of overlap of vias due to adjacent defects, the etching process was performed in three sequential intervals of 10 min each. After each interval, the samples were rinsed with deionized water and inspected under an optical microscope (Zeiss Stemi 2000C, Oberkochen, Germany).

2.3. Accelerated Aging

For encapsulation materials with very good barrier properties, such as Parylene, evaluating long-term degradation under physiological conditions (e.g., at 37 °C) typically requires years [8]. To overcome this, an accelerated aging test was performed by using higher soaking temperatures, in order to increase the rate of degradation. In this study, accelerated lifetime testing was conducted at 60 °C. Using higher temperatures increases the risk that phenomena not being present at 37 °C may occur and influence the test results [27]. The standard physiological temperature (37 °C) was used as the baseline temperature, and the acceleration factor (Q_{10}) was calculated based on the assumption that the reaction rate doubles for every 10 °C increase in temperature [28,29]. The Arrhenius equation was used to calculate the equivalent aging time at 37 °C:

$$Lifetime_{37°C} = Lifetime_{60°C} \times Q_{10}^{(T_{AA}-T_{RS})/10} \quad (1)$$

where $Q_{10} = 2$ (reaction rate doubles per 10 °C increase in temperature), $T_{AA} = 60$ °C (accelerated aging temperature), and $T_{RS} = 37$ °C (recommended shelf temperature–body temperature). Based on this equation, the acceleration factor (AF) is given by $AF = Q_{10}^{(T_{AA}-T_{RS})/10} = 2^{2.3} \approx 5$, indicating that aging at 60 °C proceeds approximately five times faster than at 37 °C.

2.4. Experimental Setup for EIS

EIS was conducted to evaluate the barrier properties and aging behavior of Parylene coatings. This technique is highly sensitive to variations in the electrical and ionic properties of the coating, providing valuable insights into its degradation over time [30,31]. Substrates with patterned copper covered with Parylene were immersed in PBS using the fluid container setup described earlier. To minimize evaporation and ensure consistent test conditions, the containers were sealed with aluminum lids and Kapton tape. The samples were stored at an elevated temperature of 60 °C in a digitally controlled oven (Horo Ovens, Ostfildern, Germany) to accelerate the degradation of the coatings. The PBS solution was replaced biweekly to mitigate concentration changes caused by evaporation.

EIS measurements were performed using a potentiostat (Bio-Logic VSP, Seyssinet, France), and data were recorded by EC-Lab software (V11.50). A three-electrode configuration was used with the encapsulated copper plane as the working electrode (WE), a platinum mesh as the counter electrode (CE), and Ag/AgCl (NaCl saturated) as the reference electrode (RE). All electrodes were immersed in PBS, as depicted in Figure 2. For the copper electrode initially coated with a perfect insulating layer, it is difficult to obtain a stable value of the open-circuit potential (OCP) [30]. Therefore, the OCP was determined on a bare copper sample and used for subsequent EIS measurements. The EIS measurements were performed using this OCP value as a baseline, applying a single sine wave amplitude of 50 mV with a frequency range from 300 mHz to 300 kHz, and recording 10 data points per decade. All measurements were conducted at room temperature after removing the samples from the oven and allowing them to cool down.

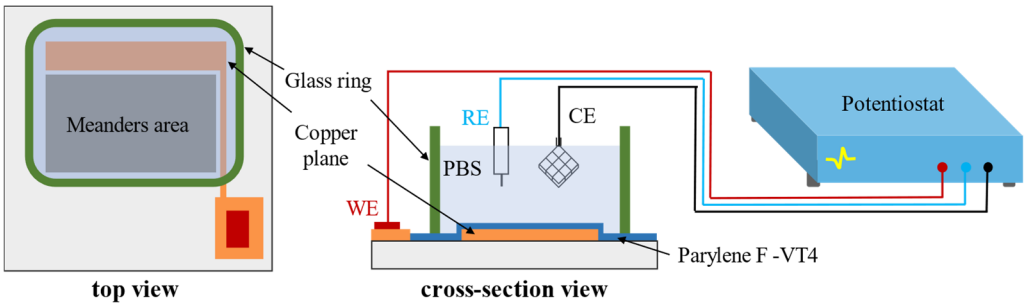

Figure 2. Schematic diagram of the electrochemical impedance spectroscopy (EIS) test setup. WE: working electrode; RE: reference electrode (Ag/AgCl); CE: counter electrode (Pt mesh).

2.5. Equivalent Circuit Modeling

Figure 3 illustrates the Cu plane coated with Parylene in a PBS solution at 3 different stages, along with the corresponding equivalent circuit model. Figure 3a shows the initial stage, where the Parylene coating is intact, effectively serving as a robust barrier, preventing the penetration of water and ions [32]. At this stage, the equivalent circuit consists of R_{PBS}, representing the bulk resistance of the PBS electrolyte; R_{por}, corresponding to the ohmic resistance of the intact Parylene coating; and C_{Par}, which represents the coating capacitance. The coating capacitance, determined by the dielectric behavior and thickness of the Parylene layer, is expressed as follows [21]:

$$C_{Par} = \varepsilon\varepsilon_0 \frac{A}{d} \quad (2)$$

where ε is the relative dielectric constant of the coating, ε_0 is the dielectric constant in vacuum, A is the surface area of the copper plane, and d is the thickness of the coating. At this stage, the impedance spectrum predominantly reflects a near-ideal capacitor due to the intact coating.

Figure 3b illustrates the next stage, during which the PBS solution begins to penetrate into the Parylene coating. This penetration occurs due to the presence of pinholes, microvoids, or inhomogeneities in the polymer structure [33,34]. The water uptake and ionic diffusion through these pathways lead to deviations from the ideal dielectric behavior of the coating [35]. Consequently, the coating capacitance (C_{Par}) is better represented by a constant phase element (CPE), Q_{Par}, which accounts for the non-ideal capacitive response [36]. The impedance of the CPE is described by the following:

$$Z_{CPE} = \frac{1}{Q(j\omega)^{\alpha}} \quad (3)$$

where Q is the magnitude of the CPE, α (ranging between 0 and 1) describes the deviation from the ideal capacitive behavior, $\omega = 2\pi f$ is the angular frequency, and j is the imaginary unit ($j^2 = -1$). At this stage, the circuit also includes R_{ct}, which represents the charge transfer resistance at the metal surface exposed to the ionically conducting pathway through the Parylene layer. Additionally, Q_{dl} corresponds to the double-layer capacitance at the interface, which also behaves as a CPE due to surface roughness, porosity, and other interfacial complexities. As the electrolyte penetrates the coating, the impedance spectra display a reduction in impedance, especially at low frequencies.

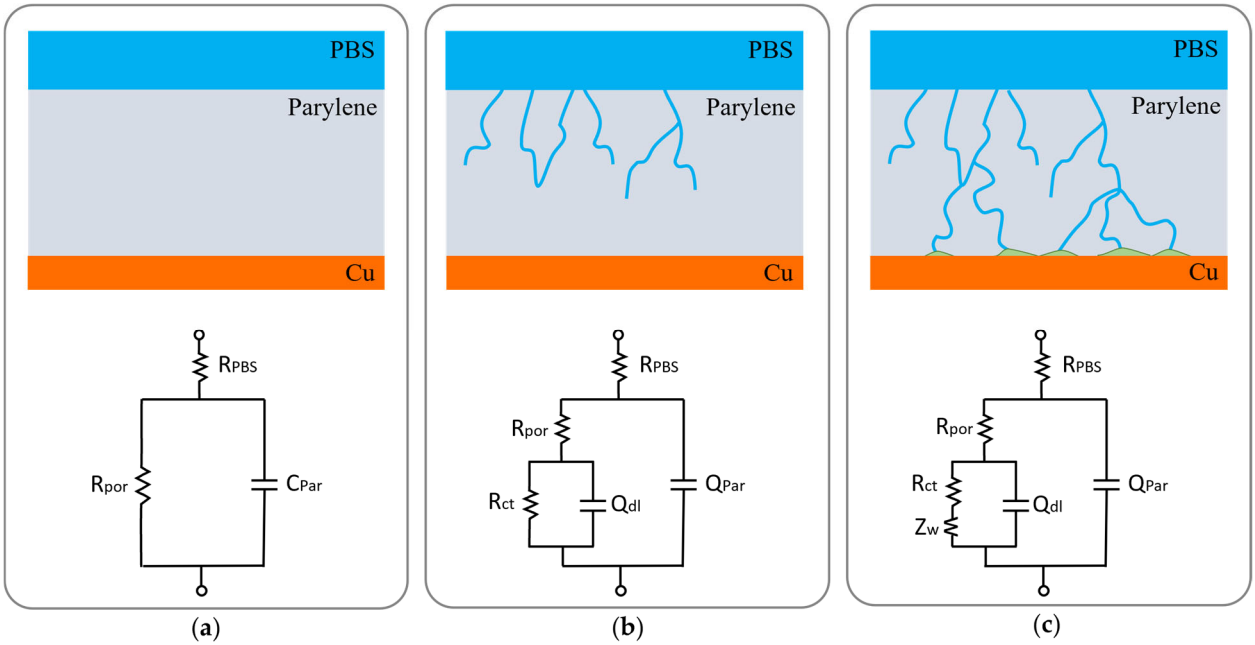

Figure 3. Temporal evolution of the Parylene F-VT4 coating in PBS, highlighting (**a**) the intact coating stage with capacitive behavior, (**b**) the intermediate stage, with water and ion penetration resulting in a non-ideal capacitance and charge transfer processes, and (**c**) the final complete coating failure leading to Cu corrosion and diffusion-dominated impedance spectra.

In the final stage (Figure 3c), the Parylene coating fails to effectively protect the copper substrate. At this stage, the PBS electrolyte has fully permeated the coating, leading to significant corrosion of the copper surface. Here, a Warburg impedance element is added to the equivalent circuit. This element accounts for the diffusion of ionic species at the metal-coating interface. The Warburg element dominates the low-frequency region of the impedance spectra, indicating (slower) diffusion-controlled processes [37]. Furthermore, the presence of corrosion products at the interface modifies the interfacial properties, adding complexity to the impedance response. Observable changes in this final stage include the dominance of the low-frequency Warburg impedance, which signifies semi-infinite diffusion behavior due to the accumulation of corrosion products and ion transport limitations. This is accompanied by a significant reduction in R_{ct}, reflecting active corrosion processes.

2.6. Resistance-Based Lifetime Testing

Cu meanders were used to evaluate the long-term performance of Parylene as an encapsulation layer by monitoring their resistance during soaking in PBS. As long as the layer functions effectively as a barrier against water and ions, the resistance of the meanders remains stable. However, when the encapsulation layer degrades, the penetration of the electrolyte into the underlying copper leads to corrosion, which causes a significant increase in resistance.

To assess the durability of Parylene coatings, resistance measurements were performed on 9 meanders present on each test substrate. These 9 meanders have 3 different widths (3 × 30 µm, 3 × 40 µm, and 3 × 50 µm). For each Parylene thickness (0.3 µm, 0.6 µm, 0.9 µm, and 1.2 µm), 3 substrates were coated and tested. Resistance measurements were recorded every six hours during soaking at 60 °C using a switching system integrated with a multimeter (Keithley 3700A, Keithley Instruments, Solon, OH, USA), ensuring precise and consistent data acquisition.

The lifetime for each meander was defined as the point when the resistance reached three times its initial value (R_0), indicating significant corrosion in meanders due to the loss of barrier integrity. Figure 4 illustrates an example of the measured resistance for a 40 µm-wide meander coated with a 0.3 µm-thick Parylene layer, showing failure at 7.5 days when the resistance increased to $3R_0$.

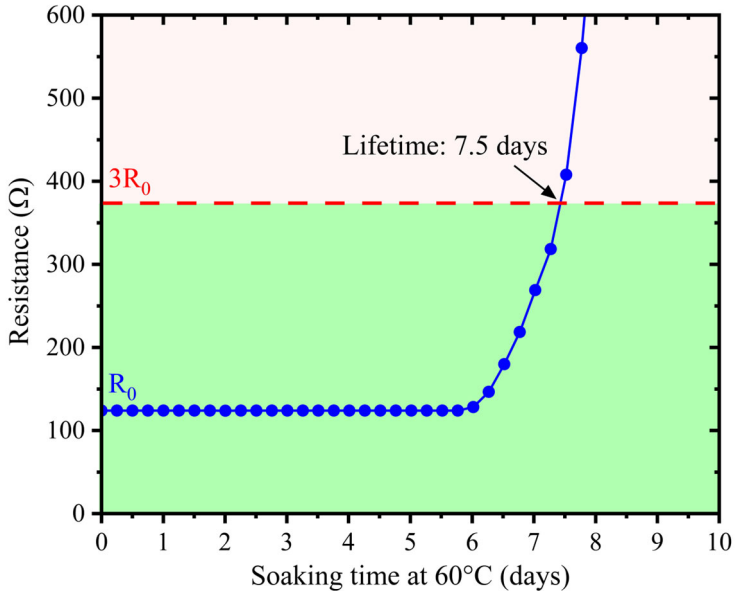

Figure 4. Resistance evolution of a 40 µm-wide meander coated with 0.3 µm Parylene F-VT4.

3. Results and Discussion

3.1. Pinhole Test

After immersion of the unpatterned copper substrates in the etching solution for 30 min in total (3 × 10 min), the created vias are counted using an optical microscope in the center area of the samples (2 cm × 2 cm). The created vias typically have a diameter between 8 µm and 15 µm, which is larger than the minimum diameter needed for proper visualization by an optical microscope. Representative images of the vias formed by Cu corrosion at pinhole locations in 0.3 µm Parylene are shown in Figure 5.

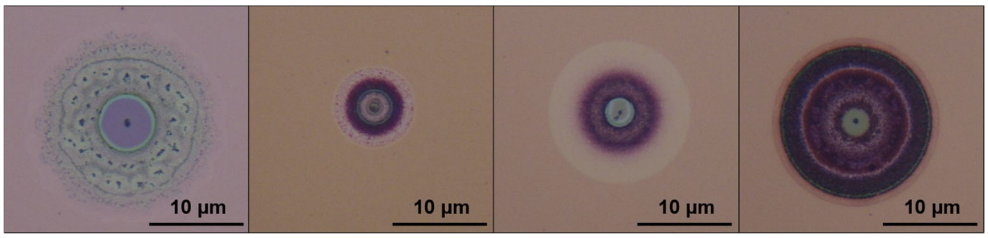

Figure 5. Optical microscope images of vias formed in the copper substrate after 30 min of etching for 0.3 µm Parylene F-VT4, highlighting pinhole defects in the layer.

Table 1 presents a summary of the results, detailing the number of pinholes detected at different time intervals for coatings with varying thicknesses. The results demonstrate a clear correlation between the coating thickness and the number of pinholes. As anticipated, the number of pinholes was greater for the 0.3 µm thick coatings compared to the 0.6 µm thick coatings. Coatings with thicknesses of 0.9 µm and 1.2 µm showed no pinholes at all.

Table 1. Number of pinholes detected (mean ± σ of three samples) at different time intervals for Parylene F-VT4 coatings of varying thicknesses.

Parylene F-VT4 Thickness	Pinhole Count (10 min)	Pinhole Count (20 min)	Pinhole Count (30 min)
0.3 µm	37 ± 3	42 ± 5	42 ± 5
0.6 µm	3 ± 1	6 ± 2	6 ± 2
0.9 µm	0	0	0
1.2 µm	0	0	0

Pinhole formation in thinner layers is typically attributed to surface contamination resulting in incomplete coverage during the deposition process, which introduces weak points in the film and hence compromises its barrier integrity. In spite of all precautions taken to avoid contamination, such as working in a cleanroom and using stringent processing protocols, the presence of surface contamination such as a small particle, a drying stain, or some chemical residues cannot be completely avoided. In such a very narrow location with surface contamination, the initial nucleation of the Parylene monomer can be inhibited during the early stages of deposition. These contaminated regions hinder initially the uniform growth of the Parylene film, leading to localized areas of non-deposition, as shown in Figure 6. Hence, for thin coatings (such as 0.3 µm), the contaminated areas remain uncovered, resulting in pinholes. The Parylene deposition process exhibits excellent step coverage; hence, when the Parylene film is growing thicker, the sidewalls of the pinholes are covered with parylene, which results in a narrowing of the pinholes, and the smallest pinholes will close, as indicated in Figure 6. For the 0.6 µm coating, the smaller pinholes are closed due to lateral film deposition, larger pinholes became smaller but remain present [38,39]. As the coating thickness increases even more, i.e., to 0.9 µm, the lateral expansion of the film is sufficient to bridge even the larger pinholes. Beyond this point, and with further increases in thickness, all pinholes are closed, and no uncovered surface regions remain. This explains the concept of a critical film thickness needed to bridge the non-nucleated regions—a threshold that depends on the contamination size and deposition parameters. One should realize, however, that even a closed pinhole can leave a local weak spot in the Parylene film, since the bottom part of the Parylene layer is locally not perfect. This highlights that substrate cleanliness is of utmost importance and that a minimum film thickness is essential to finally achieve pinhole-free Parylene coatings [40]. This minimum film thickness will be larger if the initial surface contamination is not well controlled.

3.2. EIS Results

Following the preparation of samples with different thicknesses of Parylene, EIS was performed immediately after introducing PBS into the fluid container, to evaluate the dielectric properties of the layers and to establish a baseline for subsequent aging studies. Figure 7 presents the Bode plots after immersion, highlighting the capacitive behavior of the Parylene layers. The impedance spectra demonstrate that all coatings effectively functioned as perfect dielectric barriers, with phase angles approaching −90° in the mid-frequency range, consistent with ideal capacitive behavior [41].

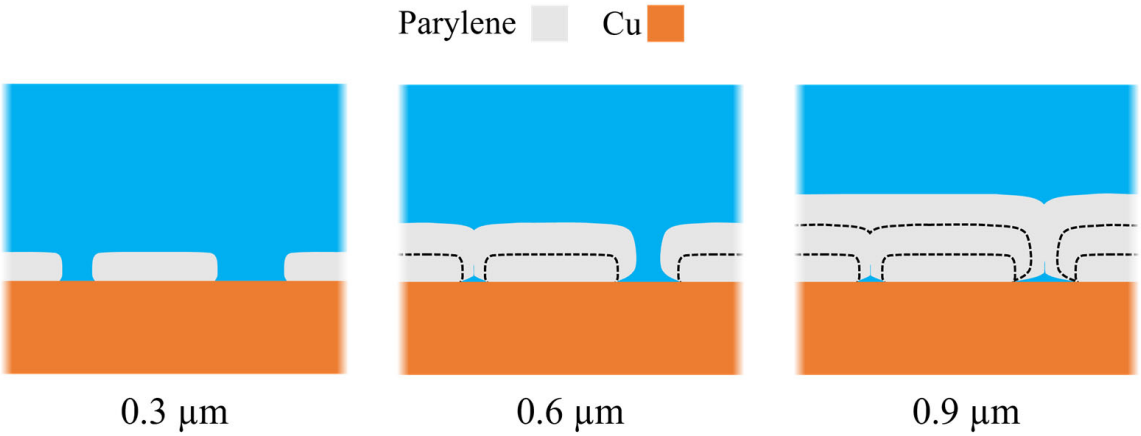

Figure 6. Origin and evolution of pinholes during Parylene deposition: poor nucleation of Parylene due to local surface contamination results in pinholes for thin Parylene layers, which will be closed when the Parylene layer gets thicker, but locally weak spots in the Parylene will remain.

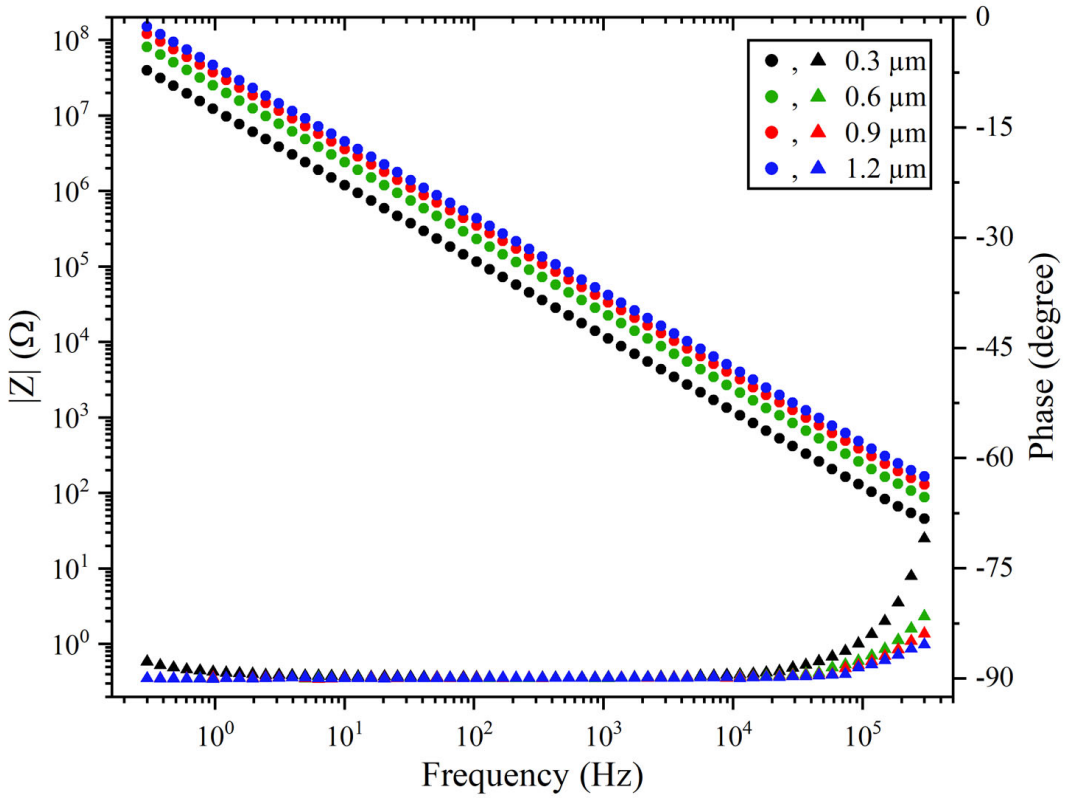

Figure 7. Magnitude (indicated by dots) and phase (indicated by triangles) of the measured impedance for four thicknesses of Parylene F-VT4 immediately after immersion in PBS.

The capacitance values of the coatings (C_{Par}) were extracted from these results using the equivalent circuit model shown in Figure 3a. Additionally, theoretical capacitance values were calculated using $C_{Par} = \varepsilon\varepsilon_0 \frac{A}{d}$, where $\varepsilon = 2.3$ is the relative dielectric constant of the coating [12], $\varepsilon_0 = 8.854 \times 10^{-12}$ F/m is the permittivity of vacuum, $A = 2 \times 10^{-4}$ m^2 is the surface area of the copper plane, and d is the Parylene thickness. Table 2 compares the calculated capacitance values with those extracted from EIS measurements, demonstrating excellent agreement between the two approaches.

Table 2. Theoretical and extracted capacitance values from different thicknesses of intact Parylene F-VT4 coatings.

Parylene F-VT4 Thickness	Extracted C_{Par} (nF)	Theoretical C_{Par} (nF)
0.3 µm	13.21	13.14
0.6 µm	6.55	6.65
0.9 µm	4.39	4.41
1.2 µm	3.50	3.45

The temporal evaluation of impedance spectra provides insight into the aging mechanism of coatings during soaking. Figure 8 illustrates the Bode plots for four thicknesses of Parylene starting immediately after immersion (0 days) until observing severe corrosion of the copper for the EIS-test substrates. For the thickest Parylene layer, the total soaking duration was ~1.5 years. EIS measurements were performed every 2 weeks, but only a selection of EIS results is shown in the plots to avoid overloading the plots while still showing the gradual change of the impedance and the phase with soaking time. Over time, a progressive decrease in impedance magnitude was observed, particularly in the low-frequency region, indicating increased ionic conduction through the coating. This behavior suggests that microvoids or defects within the Parylene structure facilitated gradual water uptake and ion diffusion. This non-ideal capacitive behavior was modeled using a constant phase element (CPE), reflecting the distribution of relaxation times due to structural inhomogeneities [42].

As is clear from the EIS results, the thickness of the Parylene coatings significantly influenced their durability, especially the 0.3 µm- and 0.6 µm-thick coatings, from which it was evident that they contained pinholes. Figure 9 shows the relative impedance and phase angle at 1 Hz during the total soaking time, for all thicknesses. The thickest coating (1.2 µm) resulted in a consistently higher impedance level for a longer soaking duration, demonstrating its superior resistance to electrolyte penetration. In contrast, thinner coatings (0.3 µm and 0.6 µm) exhibited a rapid decline in impedance, correlating with the onset of visible corrosion of the copper substrate (shown in Figure 8c,d).

The obtained impedance results were fitted using the appropriate equivalent circuit model, as shown in Figure 3. Figure 10 shows the temporal changes in the fitted circuit values of the electrical resistance of coating R_{por} and capacitance Q_{Par}. The initial R_{por} values increased significantly with coating thickness, reflecting the enhanced barrier properties of thicker layers. For the 0.3 µm coating, R_{Por} started at ~951 MΩ but decayed rapidly within the first 7 days in PBS at 60 °C, indicating swift electrolyte penetration through defects [43]. In contrast, the 0.9 µm and 1.2 µm coatings exhibited higher initial R_{Por} values and retained substantial resistance over extended soaking time, demonstrating superior protection against ion ingress. The capacitance values (Q_{Par}) provided further insights into the dielectric behavior of coatings. A slight increase in Q_{Par} was observed over time for all thicknesses, with a more significant increase for the 0.3 µm-thick Parylene coating. This behavior can be attributed to water uptake into the coating layers, which effectively increases the dielectric constant and compromises the insulating properties [44,45]. However, the decrease in Q_{Par} at later time points, especially for thinner coatings, is related to severe corrosion of the underlying copper substrate. As the copper plane corrodes, a large portion of the conductive surface is lost, reducing the effective capacitance of the test structure.

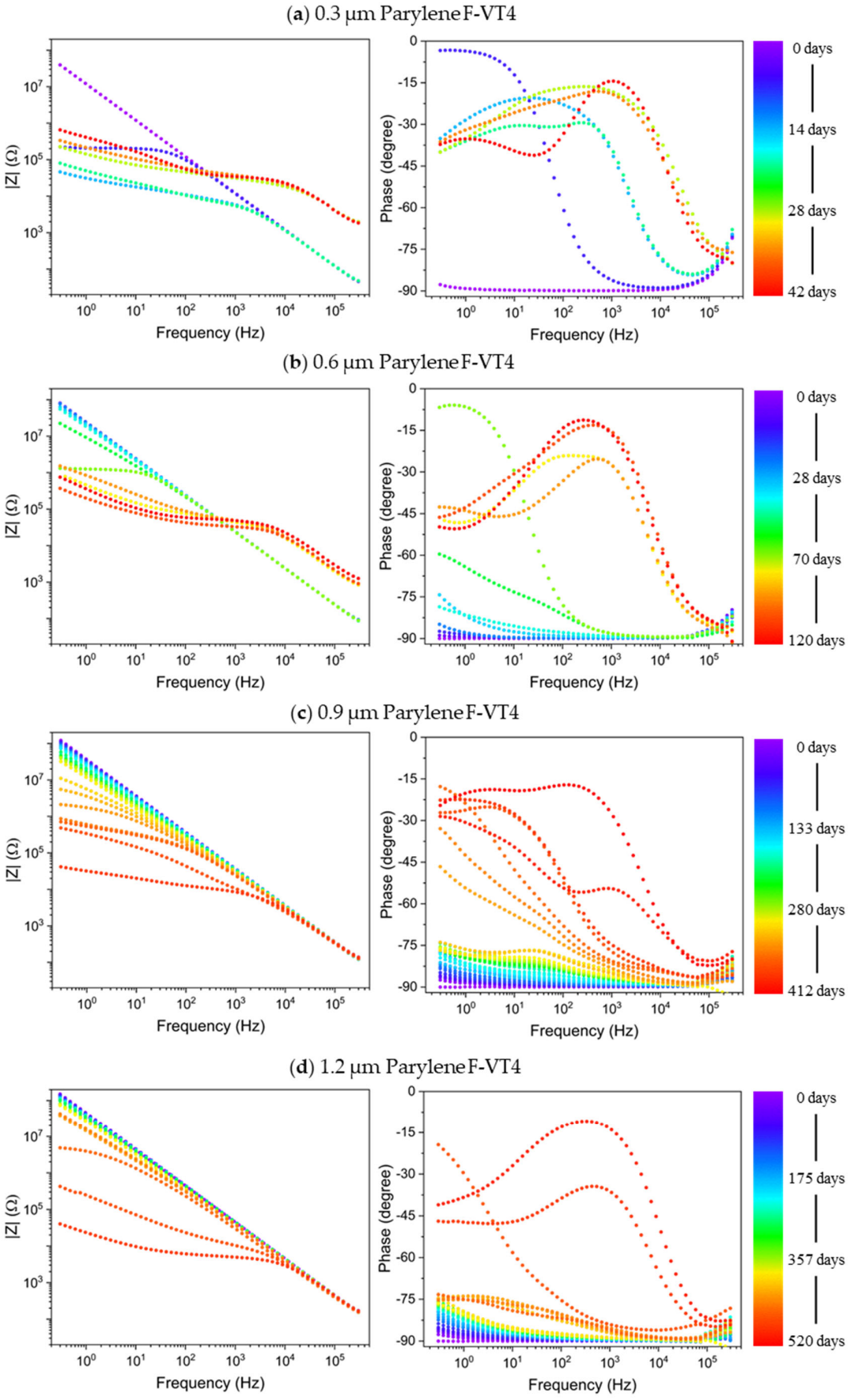

Figure 8. EIS results obtained during soaking up to 520 days: magnitude and phase of the measured impedance as a function of frequency during the soaking period.

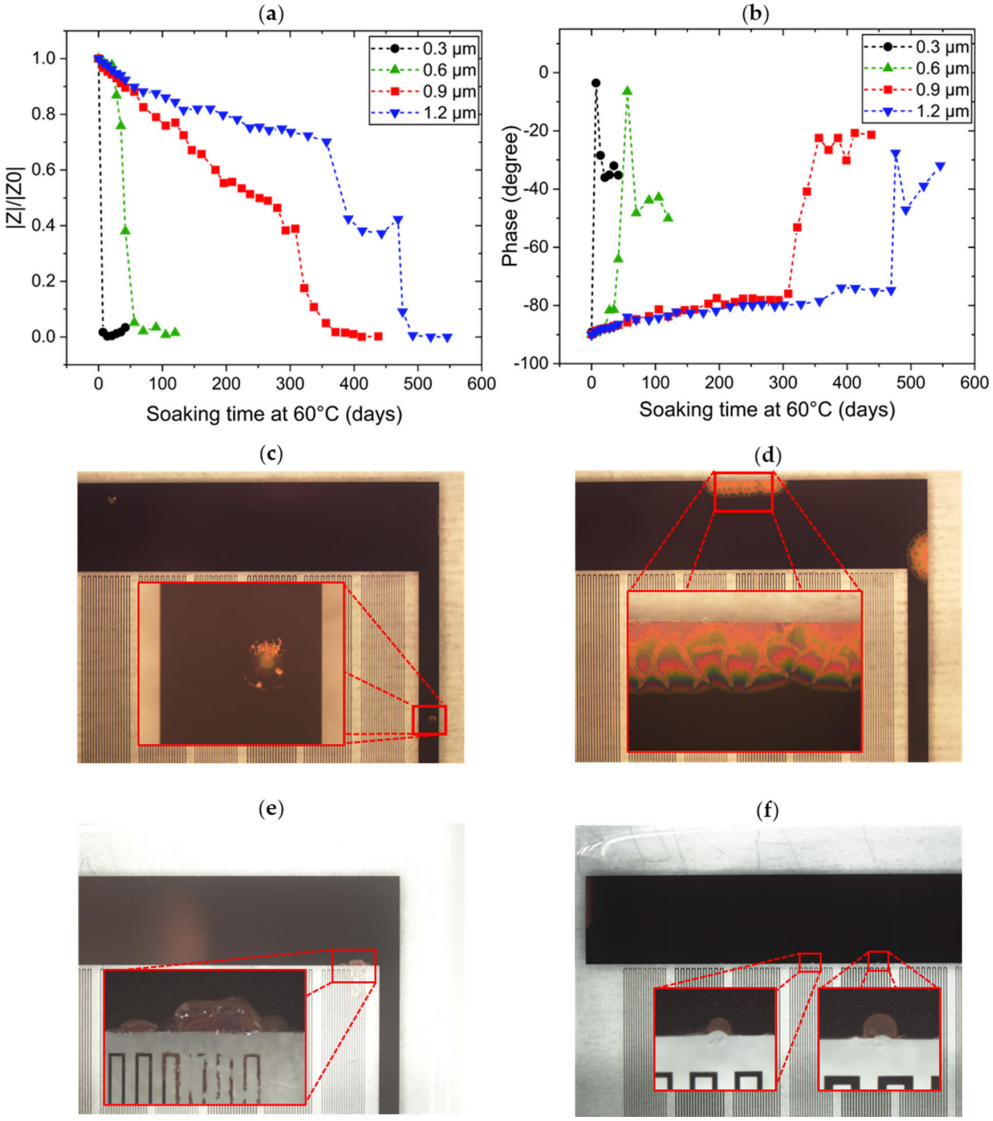

Figure 9. Evolution of the impedance modulus (**a**) and phase angle (**b**) at 1 Hz for various thicknesses of the Parylene F-VT4 coatings over the total soaking period. Failure analysis by optical microscope: image of copper plane for a 0.3 µm-thick Parylene coating at day 14 (**c**), 0.6 µm-thick Parylene coating at day 70 (**d**), 0.9 µm-thick Parylene coating at day 322 (**e**), and 1.2 µm-thick Parylene coating at day 391 (**f**).

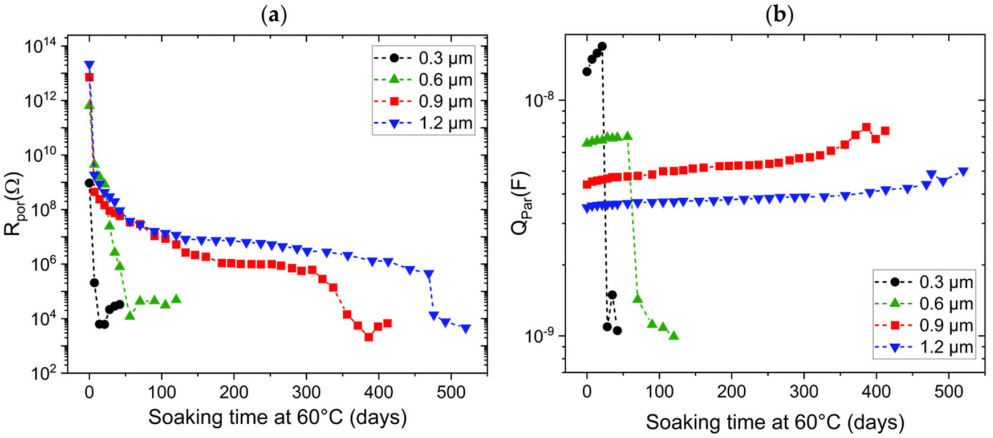

Figure 10. Temporal change in (**a**) the coating resistance (R_{por}) and (**b**) the coating capacitance (Q_{Par}) for Parylene F-VT4 layers of varying thicknesses.

3.3. Resistance-Based Lifetime Testing

As explained before, the lifetime of Cu meanders coated with Parylene was also determined when they were soaked in PBS at 60 °C. Figure 11 illustrates the resistance measurement of Cu meanders coated with 0.3 µm of Parylene. In previous work, the lifetime of bare Cu meanders in PBS at 60 °C (the same meander design as used in this work) was determined. The bare Cu patterns corroded very fast in warm PBS. The lifetime was approximately 0.73 day for 50 µm-, 0.85 day for 40 µm-, and 0.95 day for 30 µm-wide meanders [27]. The Cu meander width influenced the lifetime, but only with a few hours' difference. When looking at the results regarding similar Cu meanders but covered with 0.3 µm of Parylene, a much longer lifetime was observed, with times to failure between 5 days and 16 days. The variation in lifetime between the meanders is large but is no longer dependent on meander width. Optical images of 0.3 µm-thick Parylene-coated meanders, after 7 days and 14 days of soaking, are shown in Figure 12. As indicated in these images, corrosion of Cu begins very locally at all positions where the Parylene coating has a weaker spot due to a local pinhole/defect. Since a 0.3 µm-thick Parylene coating still has a lot of pinholes/defects, corrosion starts for all meanders at various positions between day 3 and day 14. The onset of corrosion can be slightly delayed if the pinhole/defect is smaller, but after 14 days, all meanders have areas where PBS could penetrate through the Parylene layer, leading to local corrosion. This mechanism is referred to as 'primary corrosion' in this work.

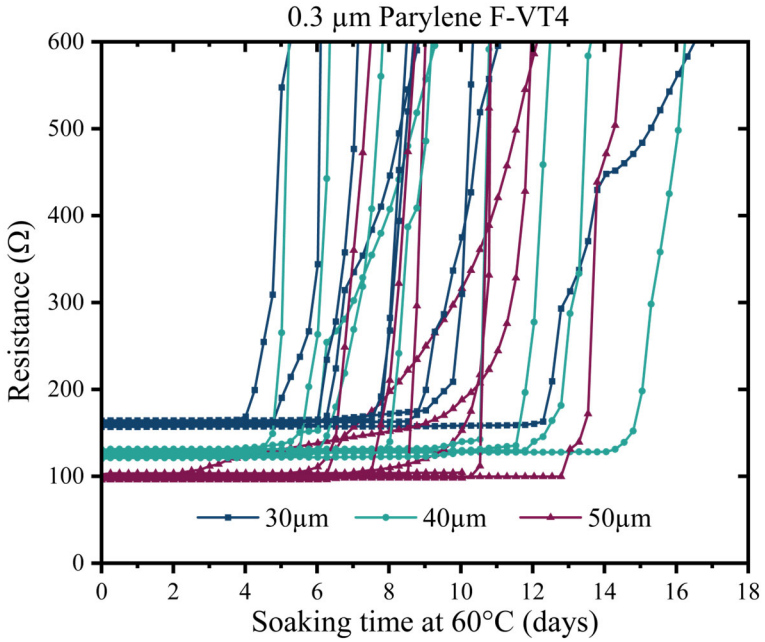

Figure 11. Change in resistance of 30 µm-, 40 µm-, and 50 µm-wide meanders coated with 0.3 µm-thick Parylene F-VT4 layers during soaking in PBS at 60 °C.

When primary corrosion starts, the corrosion products locally cause a volume increase, which locally exerts increased pressure at the Cu–Parylene interface. Depending on the adhesion of the Parylene layer to the Cu, the Parylene layer will locally peel off from the substrate, creating more Cu area that is directly exposed to moisture and ions [46,47]. This novel exposed Cu will corrode and will lead to even more Cu corrosion products, contributing to an even higher local interfacial pressure, further damaging the Cu–Parylene interface even more, causing again novel Cu areas exposed to moisture and ions, etc. This effect is referred to as 'lateral corrosion' throughout the text, and the mechanism of primary corrosion followed by lateral corrosion is schematically explained in Figure 13. Due to

this primary corrosion followed by lateral corrosion, the resistance of a Cu meander is increasing, until the lifetime criterion ($3 \times R_0$) is reached.

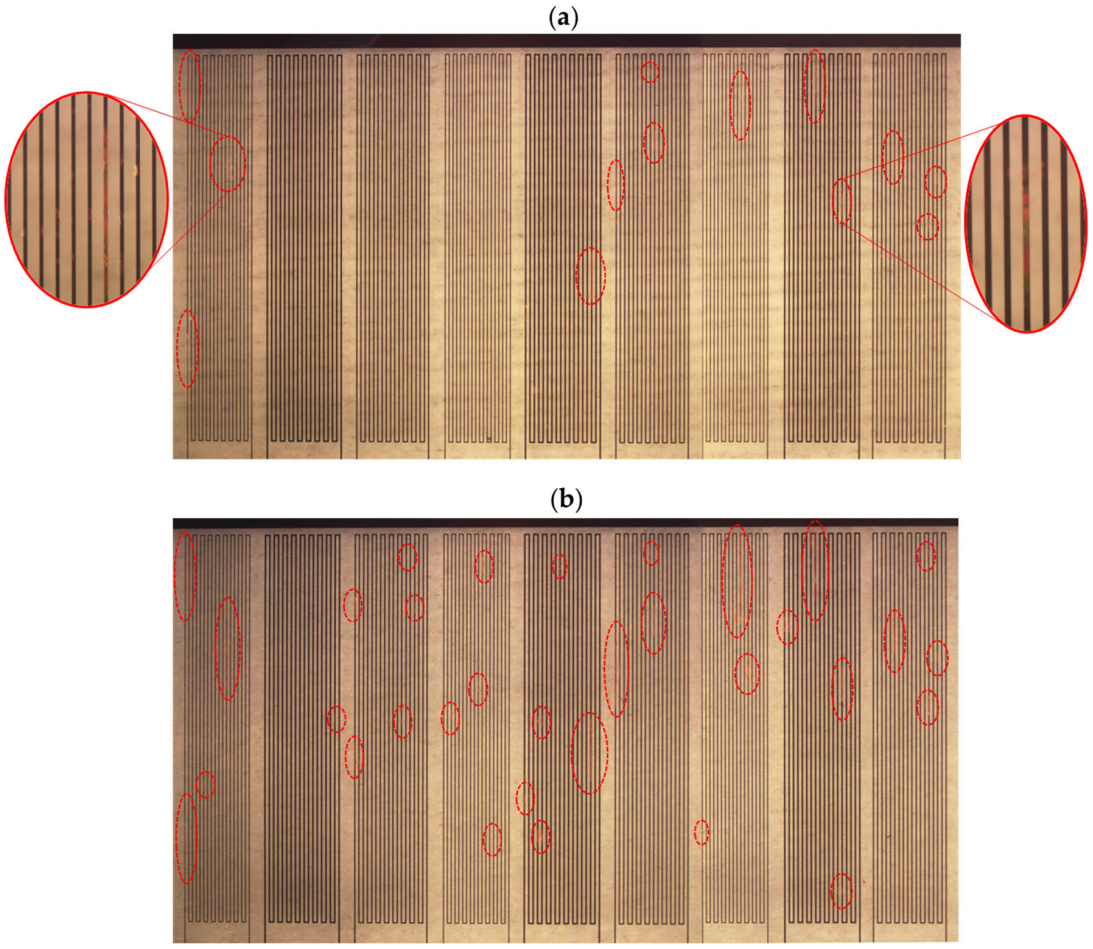

Figure 12. Optical images of meanders coated with a 0.3 µm-thick layer of Parylene F-VT4. Corroded areas are indicated by red ellipses: (**a**) after 7 days, (**b**) after 14 days.

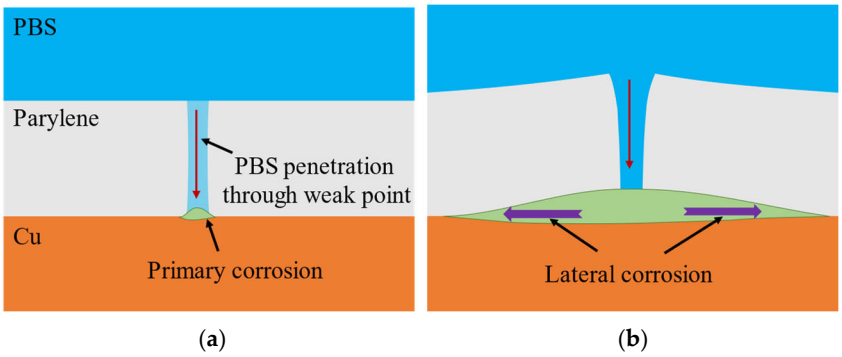

Figure 13. Two failure mechanisms for Cu meanders: (**a**) primary corrosion caused by weak points in the Parylene layers and (**b**) lateral corrosion resulting from volume expansion by corrosion products.

Also, for meanders covered with thicker layers of Parylene (>0.3 µm), these two distinct corrosion mechanisms were observed. However, with increasing thickness of Parylene, the amount of weak Parylene areas due to defects/pinholes decreases. This results in fewer positions that will suffer from primary corrosion. As a consequence, lateral corrosion will become a very important contributor to the lifetime of the meanders. To explain this in more detail, we will look at the Cu meanders coated with a 0.9 µm-thick

Parylene layer. Figure 14 shows optical images of these meanders after various soaking times in PBS at 60 °C. As shown in Figure 14a, after 197 days, two meanders are corroded due to primary corrosion, as indicated by the red ellipses. This primary corrosion originates from weak points in the 0.9 µm-thick Parylene coating causing electrolyte penetration until the underlying copper pattern is reached. As explained before, corrosion products cause increased stress at the interface, resulting in local delamination of the Parylene coating, which enables lateral electrolyte penetration followed by extra corrosion of newly exposed copper areas. Initially, this lateral corrosion will happen at the same Cu meander, but after some time, this lateral corrosion will also reach the other meander patterns located left and/or right from the meander that suffers from primary corrosion (as shown in Figure 14). After some time, the neighboring meanders will suffer so much from lateral corrosion that they are completely damaged and their lifetime is reached. If meanders reach their lifetime due to lateral corrosion only, we will call this failure mechanism of the meander 'secondary corrosion'. The thicker the Parylene layer on top of the meanders, the fewer weak spots are present in the Parylene layer, hence fewer meanders will fail due to primary corrosion, and more meanders will fail due to secondary corrosion. When neighboring meanders corrode and reach their lifetime due to secondary corrosion, this is not related to the Parylene coating quality, but to the adhesion between the Parylene and the underlying materials. Weaker adhesion will result in a faster lateral corrosion process. Also, the pattern design plays a role: a design with more area of copper will result in more corrosion products, which will generate more interfacial stress and hence a faster progress of the lateral corrosion. If the distance between the meanders in our design were increased, the lateral corrosion would be slowed down severely, and neighboring meanders would only start to suffer from lateral corrosion after a much longer time. Although both primary and secondary corrosion ultimately results in meanders reaching their lifetime, it is important to distinguish between the two failure mechanisms due to their difference in origin.

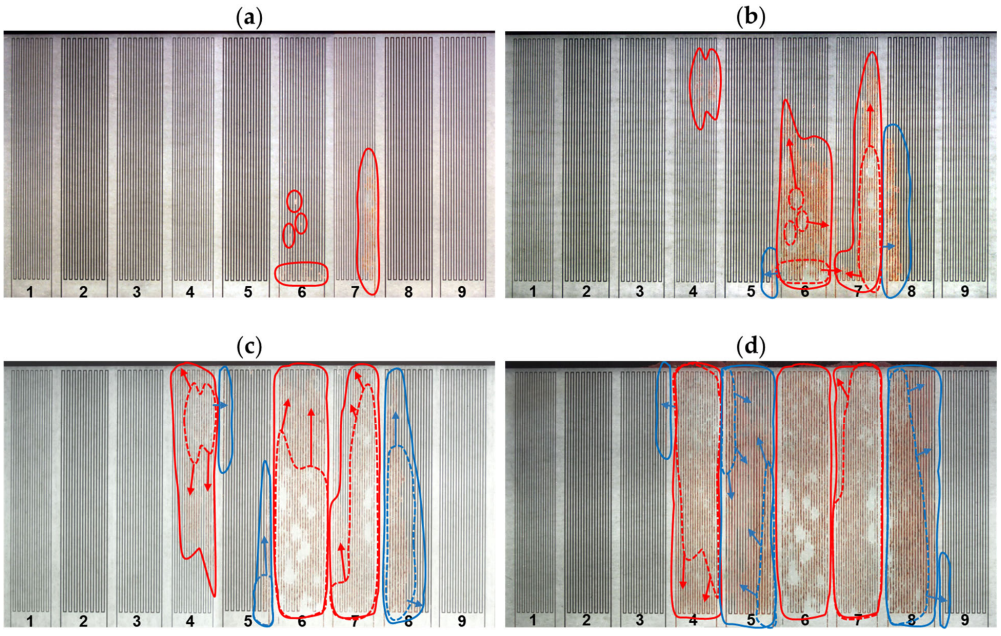

Figure 14. Optical images of meanders coated with 0.9 µm-thick Parylene F-VT4: (**a**) after 197 days, meanders 6 and 7 showed signs of primary corrosion, (**b**) after 245 days, meander 4 also showed primary corrosion, while meanders 5 and 8 showed secondary corrosion, (**c**) after 273 days, (**d**) after 307 days, meanders 3 and 9 showed secondary corrosion. Arrows indicate the direction of lateral corrosion. The red solid lines indicate the corroded area due to primary corrosion, and the blue solid lines indicate the corroded area due to secondary corrosion. Dashed lines indicate the previously corroded areas.

The presence of lateral corrosion reduces the meander's lifetime but is not a function of the local Parylene integrity; hence, it is not a function of the Parylene thickness. The progress of lateral corrosion mainly depends on the adhesion of Parylene on Cu and glass. Probably the Cu thickness also plays a role, since a thicker Cu layer results in more local corrosion products; hence, a larger volume of corrosion products will push the Parylene layer upward. Hence, when looking at the obtained lifetime of all meanders present on a substrate, we cannot avoid mixing two failure mechanisms: (1) primary corrosion influenced strongly by parylene thickness, and (2) secondary corrosion influenced by the Cu pattern design, the adhesion of the Parylene, and probably also the Cu thickness. We calculated the lifetime for each meander based on the $3R_0$ method, but simultaneously we classified for each meander the occurring failure mechanism based on optical microscope images taken at regular time intervals during the immersion of the test structures in PBS. In Figure 15a, we plotted only the resistance results for meanders that failed due to primary corrosion for all Parylene thicknesses. As expected, meanders coated with thicker Parylene layers exhibit a longer lifetime. Figure 15b shows the number of meanders failing by primary and secondary corrosion for the four different thicknesses of Parylene. This graph illustrates clearly that the number of meanders failing due to primary corrosion decreased as the thickness of Parylene increased. As mentioned before, all meanders coated with 0.3 µm-thick Parylene fail due to primary corrosion. The observed reduction in the number of meanders failing by primary corrosion as the coating thickness increases indicates a decrease in the density of weak points within the coating layer.

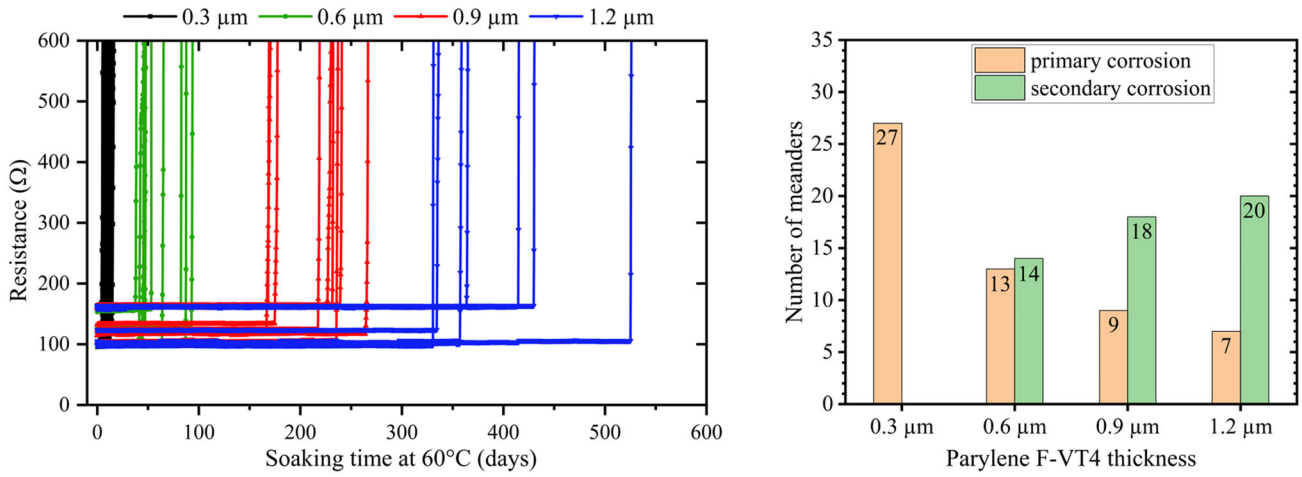

Figure 15. (**a**) Resistance values of meanders coated with different thicknesses of Parylene F-VT4 during soaking in PBS at 60 °C; only meanders failing due to primary corrosion are shown. (**b**) Comparison of meanders failing due to primary and secondary corrosion for different thicknesses of Parylene F-VT4 during soaking in PBS at 60 °C.

Figure 16 shows the time to failure of meanders for all samples, failing by both primary and lateral corrosion mechanisms. All meanders coated with 0.3 µm-thick Parylene failed after 16 days of soaking in PBS at 60 °C. Meanders coated with 0.6 µm-thick Parylene began to fail after 39 days, with all failures occurring by 107 days of soaking. Meanders coated with 0.9 µm-thick Parylene did not fail until 169 days, and all 27 meanders failed after 436 days. For meanders encapsulated with 1.2 µm-thick Parylene, failure began after 331 days, with failure of all meanders after 550 days.

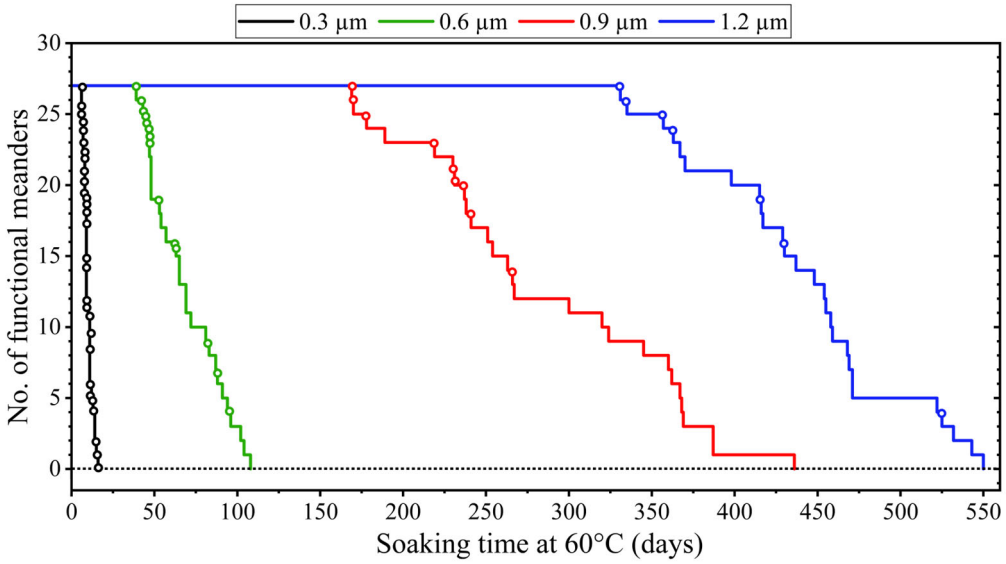

Figure 16. The time to failure of meanders coated with different thicknesses of Parylene F-VT4 during soaking in PBS at 60 °C, taking into account meanders failing due to both primary and secondary corrosion. Meanders corroded by primary corrosion are indicated by small circles.

3.4. Mean Time to Failure and Lifetime

Since secondary corrosion is not directly related to the quality of the encapsulation layer, for the calculation of the lifetime of Parylene, we only considered meanders that failed due to primary corrosion. Therefore, after extracting the lifetime for each meander based on the $3R_0$ method, we report the average lifetime of only the meanders that failed due to only primary corrosion as the mean time to failure (MTTF). Table 3 shows the MTTF at 60 °C and the MTTF at 37 °C, extrapolated using Equation (1). The MTTF analysis highlights the critical influence of Parylene thickness on its durability and failure time. For the thinnest coating (0.3 µm thickness), the MTTF was approximately 9.4 days at 60 °C, corresponding to an extrapolated lifetime of about 1.5 months at 37 °C. This limited durability reflects the vulnerability of the ultrathin barrier to electrolyte penetration due to the presence of pinholes, which rapidly compromise its protective properties. Increasing the coating thickness to 0.6 µm resulted in a significant improvement, with an MTTF of approximately 9.5 months at 37 °C. This enhancement reflects a reduction in pinhole density and improved barrier integrity, demonstrating that increased thickness effectively mitigates structural defects. A further increase in thickness to 0.9 µm and 1.2 µm yielded substantial performance gains, with extrapolated MTTFs of approximately 3 years and 5.5 years at 37 °C, respectively. The absence of pinholes in these thicknesses, coupled with the high barrier properties of Parylene F-VT4 against electrolyte diffusion, significantly enhanced their effectiveness in preventing electrolyte penetration and reinforced their reliability as encapsulation layers. It is important to note that the MTTF is related to the surface area of meanders, which is approximately 0.4 cm^2 for this study. The number of pinholes present in a Parylene layer is obviously a function of the Parylene thickness but also of the area, characterized by pinhole density. For samples that occupy less surface areas, the MTTF will typically be higher.

In this study, the lifetime of the Parylene layer is determined by the failure time of the first meanders to fail, rather than the MTTF across all meanders. The timing of the first failure is the critical point that dictates the actual operational life of the encapsulation in realistic applications. Therefore, the lifetime of the Parylene layers was determined by the time to failure of the first meander within each thickness group. The lifetime at 60 °C and

the extrapolated lifetime at 37 °C are shown in Table 4 for all four thicknesses of Parylene. The results show a clear correlation between the Parylene thickness and the lifetime.

Table 3. Mean time to failure of four thicknesses of Parylene F-VT4.

Parylene F-VT4 Thickness	MTTF at 60 °C (Days) Mean ± σ	Extrapolated MTTF at 37 °C (Q_{10} = 2)
0.3 µm	9.4 ± 2.8	~1.5 months
0.6 µm	57 ± 18.6	~9.5 months
0.9 µm	215.4 ± 34.8	~3 years
1.2 µm	393.7 ± 69	~5.5 years

Table 4. Lifetime of four thicknesses of Parylene F-VT4.

Parylene F-VT4 Thickness	Lifetime at 60 °C (Days)	Extrapolated Lifetime at 37 °C (Q_{10} = 2)
0.3 µm	5	~25 days
0.6 µm	38	~6.4 months
0.9 µm	169	~2.3 years
1.2 µm	331	~4.5 years

Obviously, these lifetime values are strongly related to the test structure, being a flat Cu-on-glass device with meanders having a surface area of ~0.4 cm^2. We have chosen Cu as the test material, which corrodes very fast, in order to perform our evaluation of Parylene with a sensitive test structure. A real implant will be a three-dimensional device with other dimensions, consisting of many materials, often less sensitive to corrosion than Cu. Hence, for each implant, the lifetime of a Parylene F-VT4 barrier coating needs to be tested. However, the fact that a lifetime of several years can be obtained on our sensitive Cu structures is very promising.

4. Conclusions

This study examined the performance of Parylene F-VT4 coatings of varying thicknesses as protective encapsulation layers for implantable medical devices, with a focus on understanding how the thickness of the barrier layer influences its performance. The coatings were evaluated using three techniques: pinhole density measurements, electrochemical impedance spectroscopy (EIS), and resistance-based lifetime testing. Thinner coatings (0.3 µm and 0.6 µm thickness) showed rapid degradation and short lifetime due to the presence of pinholes. These pinholes allow electrolytes to reach the underlying substrate. In contrast, thicker coatings (0.9 µm and 1.2 µm thickness) that are free of pinholes exhibit superior barrier properties compared to the thinner layers.

In conclusion, Parylene F-VT4 coatings with thicknesses of 0.9 µm and 1.2 µm could be good candidates for encapsulation of implantable medical devices with an implantation duration of a few years. Our results showed a lifetime of almost 6 months for the 0.9 µm coating and approximately 11 months for the 1.2 µm coating at 60 °C in PBS. This corresponds to a calculated lifetime at 37 °C of approximately 2.3 years for the 0.9 µm-thick coating and approximately 4.5 years for the 1.2 µm-thick coating. While these results are based on simplified test structures, they suggest that these coatings could work well for real implants. If better barrier properties are needed, combining Parylene F-VT4 coatings with inorganic nanolayers deposited by atomic layer deposition could provide an effective ultra-long-term encapsulation solution.

Author Contributions: Conceptualization, E.A. and M.O.d.B.; methodology, E.A., R.V. and M.C.; validation, E.A., R.V. and M.O.d.B.; formal analysis, E.A.; investigation, E.A.; data curation, E.A.; writing—original draft preparation, E.A.; writing—review and editing, R.V., M.C. and M.O.d.B.; supervision, M.O.d.B.; funding acquisition, M.O.d.B. All authors have read and agreed to the published version of the manuscript.

Funding: This research received no external funding.

Institutional Review Board Statement: Not applicable.

Informed Consent Statement: Not applicable.

Data Availability Statement: Data are contained within the article.

Acknowledgments: We would like to thank Lothar Mader, Filip Vermeiren, and Kristof Dhaenens for their invaluable assistance with sample preparation and Parylene F-VT4 deposition for this study.

Conflicts of Interest: The authors declare no conflicts of interest.

References

1. Khan, W.; Muntimadugu, E.; Jaffe, M.; Domb, A.J. Implantable Medical Devices. In *Focal Controlled Drug Deliver*; Springer: Boston, MA, USA, 2014; pp. 33–59.
2. Bazaka, K.; Jacob, M.V. Implantable Devices: Issues and Challenges. *Electronics* **2012**, *2*, 1–34. [CrossRef]
3. Cho, Y.U.; Lim, S.L.; Hong, J.-H.; Yu, K.J. Transparent Neural Implantable Devices: A Comprehensive Review of Challenges and Progress. *npj Flex. Electron.* **2022**, *6*, 53. [CrossRef]
4. Sang, M.; Kim, K.; Shin, J.; Yu, K.J. Ultra-thin Flexible Encapsulating Materials for Soft Bio-integrated Electronics. *Adv. Sci.* **2022**, *9*, 2202980. [CrossRef] [PubMed]
5. Mariello, M.; Kim, K.; Wu, K.; Lacour, S.P.; Leterrier, Y. Recent Advances in Encapsulation of Flexible Bioelectronic Implants: Materials, Technologies, and Characterization Methods. *Adv. Mater.* **2022**, *34*, 2201129. [CrossRef]
6. Ahn, S.-H.; Jeong, J.; Kim, S.J. Emerging Encapsulation Technologies for Long-Term Reliability of Microfabricated Implantable Devices. *Micromachines* **2019**, *10*, 508. [CrossRef]
7. Kim, S.H.; Moon, J.-H.; Kim, J.H.; Jeong, S.M.; Lee, S.-H. Flexible, Stretchable and Implantable PDMS Encapsulated Cable for Implantable Medical Device. *Biomed. Eng. Lett.* **2011**, *1*, 199–203. [CrossRef]
8. Hsu, J.-M.; Rieth, L.; Normann, R.A.; Tathireddy, P.; Solzbacher, F. Encapsulation of an Integrated Neural Interface Device with Parylene C. *IEEE Trans. Biomed. Eng.* **2008**, *56*, 23–29. [CrossRef]
9. Caldwell, R.; Street, M.G.; Sharma, R.; Takmakov, P.; Baker, B.; Rieth, L. Characterization of Parylene-C Degradation Mechanisms: In Vitro Reactive Accelerated Aging Model Compared to Multiyear In Vivo Implantation. *Biomaterials* **2020**, *232*, 119731. [CrossRef]
10. Golda-Cepa, M.; Engvall, K.; Hakkarainen, M.; Kotarba, A. Recent Progress on Parylene C Polymer for Biomedical Applications: A Review. *Prog. Org. Coat.* **2020**, *140*, 105493. [CrossRef]
11. Vaeth, K.M.; Jensen, K.F. Transition Metals for Selective Chemical Vapor Deposition of Parylene-Based Polymers. *Chem. Mater.* **2000**, *12*, 1305–1313. [CrossRef]
12. Kahouli, A.; Sylvestre, A.; Laithier, J.-F.; Lutsen, L.; Pairis, S.; André, E.; Garden, J.-L. Structural and Dielectric Properties of Parylene-VT4 Thin Films. *Mater. Chem. Phys.* **2014**, *143*, 908–914. [CrossRef]
13. Buchwalder, S.; Borzì, A.; Diaz Leon, J.J.; Bourgeois, F.; Nicolier, C.; Nicolay, S.; Neels, A.; Zywitzki, O.; Hogg, A.; Burger, J. Thermal Analysis of Parylene Thin Films for Barrier Layer Applications. *Polymers* **2022**, *14*, 3677. [CrossRef] [PubMed]
14. Tipnis, N.P.; Burgess, D.J. Sterilization of Implantable Polymer-Based Medical Devices: A Review. *Int. J. Pharm.* **2018**, *544*, 455–460. [CrossRef] [PubMed]
15. Li, C.; Cauwe, M.; Yang, Y.; Schaubroeck, D.; Mader, L.; Op de Beeck, M. Ultra-Long-Term Reliable Encapsulation Using an Atomic Layer Deposited $HfO_2/Al_2O_3/HfO_2$ Triple-Interlayer for Biomedical Implants. *Coatings* **2019**, *9*, 579. [CrossRef]
16. Li, C.M.; Dong, H.; Cao, X.; Luong, J.H.; Zhang, X. Implantable Electrochemical Sensors for Biomedical and Clinical Applications: Progress, Problems, and Future Possibilities. *Curr. Med. Chem.* **2007**, *14*, 937–951.
17. Baxter, L.K. *Capacitive Sensors: Design and Applications*; IEEE: New York, NY, USA, 1997.
18. Daniels, J.S.; Pourmand, N. Label-free Impedance Biosensors: Opportunities and Challenges. *Electroanal. Int. J. Devoted Fundam. Pract. Asp. Electroanal.* **2007**, *19*, 1239–1257. [CrossRef]
19. Oevermann, J.; Weber, P.; Tretbar, S.H. Encapsulation of Capacitive Micromachined Ultrasonic Transducers (CMUTs) for the Acoustic Communication between Medical Implants. *Sensors* **2021**, *21*, 421. [CrossRef]

20. Yaacob, M.I.H.; Arshad, M.R.; Manaf, A.A.; Rahman, M.F.A.; Samsuri, S.S. Enhancement of Piezoelectric Micromachined Ultrasonic Transducer Using Polymer Membrane for Underwater Applications. *Indian J. Mar. Sci.* **2012**, *41*, 533–539.
21. Grundmeier, G.; Schmidt, W.; Stratmann, M. Corrosion Protection by Organic Coatings: Electrochemical Mechanism and Novel Methods of Investigation. *Electrochim. Acta* **2000**, *45*, 2515–2533. [CrossRef]
22. Deflorian, F.; Rossi, S. An EIS Study of Ion Diffusion through Organic Coatings. *Electrochim. Acta* **2006**, *51*, 1736–1744. [CrossRef]
23. Castela, A.S.L.; Simoes, A.M.; Ferreira, M.G.S. EIS Evaluation of Attached and Free Polymer Films. *Prog. Org. Coat.* **2000**, *38*, 1–7. [CrossRef]
24. Lyon, S.B.; Bingham, R.; Mills, D.J. Advances in Corrosion Protection by Organic Coatings: What We Know and What We Would like to Know. *Prog. Org. Coat.* **2017**, *102*, 2–7. [CrossRef]
25. Zhang, Y.; Bertrand, J.A.; Yang, R.; George, S.M.; Lee, Y.C. Electroplating to Visualize Defects in Al_2O_3 Thin Films Grown Using Atomic Layer Deposition. *Thin Solid Film.* **2009**, *517*, 3269–3272. [CrossRef]
26. Vanhaverbeke, C.; Cauwe, M.; Stockman, A.; de Beeck, M.O.; De Smet, H. Comparison of Copper Electroplating, Copper Wet Etching and Linear Sweep Voltammetry as Techniques to Investigate the Porosity of Atomic Layer Deposited Al_2O_3. *Thin Solid Film.* **2019**, *686*, 137424. [CrossRef]
27. Li, C.; Cauwe, M.; Mader, L.; Schaubroeck, D.; Op de Beeck, M. Accelerated Hermeticity Testing of Biocompatible Moisture Barriers Used for the Encapsulation of Implantable Medical Devices. *Coatings* **2019**, *10*, 19. [CrossRef]
28. Hukins, D.W.L.; Mahomed, A.; Kukureka, S.N. Accelerated Aging for Testing Polymeric Biomaterials and Medical Devices. *Med. Eng. Phys.* **2008**, *30*, 1270–1274. [CrossRef]
29. Hemmerich, K.J. General Aging Theory and Simplified Protocol for Accelerated Aging of Medical Devices. *Med. Plast. Biomater.* **1998**, *5*, 16–23.
30. Loveday, D.; Peterson, P.; Rodgers, B. Evaluation of Organic Coatings with Electrochemical Impedance Spectroscopy. *JCT Coat. Tech.* **2004**, *8*, 46–52.
31. Van Westing, E.P.M.; Ferrari, G.M.; De Wit, J.H.W. The Determination of Coating Performance Using Electrochemical Impedance Spectroscopy. *Electrochim. Acta* **1994**, *39*, 899–910. [CrossRef]
32. Fernández-Sánchez, C.; McNeil, C.J.; Rawson, K. Electrochemical Impedance Spectroscopy Studies of Polymer Degradation: Application to Biosensor Development. *TrAC Trends Anal. Chem.* **2005**, *24*, 37–48. [CrossRef]
33. González-Hernández, A.; Morales-Cepeda, A.B.; Flores, M.; Caicedo, J.C.; Aperador, W.; Amaya, C. Electrochemical Properties of TiWN/TiWC Multilayer Coatings Deposited by RF-Magnetron Sputtering on AISI 1060. *Coatings* **2021**, *11*, 797. [CrossRef]
34. Chun, W.; Chou, N.; Cho, S.; Yang, S.; Kim, S. Evaluation of Sub-Micrometer Parylene C Films as an Insulation Layer Using Electrochemical Impedance Spectroscopy. *Prog. Org. Coat.* **2014**, *77*, 537–547. [CrossRef]
35. Brasher, D.M.; Kingsbury, A.H. Electrical Measurements in the Study of Immersed Paint Coatings on Metal. I. Comparison between Capacitance and Gravimetric Methods of Estimating Water-uptake. *J. Appl. Chem.* **1954**, *4*, 62–72. [CrossRef]
36. Minnikanti, S.; Diao, G.; Pancrazio, J.J.; Xie, X.; Rieth, L.; Solzbacher, F.; Peixoto, N. Lifetime Assessment of Atomic-Layer-Deposited Al_2O_3–Parylene C Bilayer Coating for Neural Interfaces Using Accelerated Age Testing and Electrochemical Characterization. *Acta Biomater.* **2014**, *10*, 960–967. [CrossRef]
37. Mengesha, G.A.; Chu, J.P.; Lou, B.-S.; Lee, J.-W. Corrosion Performance of Plasma Electrolytic Oxidation Grown Oxide Coating on Pure Aluminum: Effect of Borax Concentration. *J. Mater. Res. Technol.* **2020**, *9*, 8766–8779. [CrossRef]
38. Gao, Z.; Jiang, Y.; Meng, Y.; Du, M.; Liu, F. A Review of the Fabrication of Pinhole-Free Thin Films Based on Electrodeposition Technology: Theory, Methods and Progress. *Molecules* **2024**, *29*, 5615. [CrossRef]
39. Panjan, P.; Drnovšek, A.; Gselman, P.; Čekada, M.; Panjan, M. Review of Growth Defects in Thin Films Prepared by PVD Techniques. *Coatings* **2020**, *10*, 447. [CrossRef]
40. Camacho-Espinosa, E.; Oliva-Avilés, A.I.; Oliva, A.I. Effect of the Substrate Cleaning Process on Pinhole Formation in Sputtered CdTe Films. *J. Mater. Eng. Perform.* **2017**, *26*, 4020–4028. [CrossRef]
41. Trentin, A.; Pakseresht, A.; Duran, A.; Castro, Y.; Galusek, D. Electrochemical Characterization of Polymeric Coatings for Corrosion Protection: A Review of Advances and Perspectives. *Polymers* **2022**, *14*, 2306. [CrossRef]
42. Margarit-Mattos, I.C.P. EIS and Organic Coatings Performance: Revisiting Some Key Points. *Electrochim. Acta* **2020**, *354*, 136725. [CrossRef]
43. Pokhodnya, K.I.; Bonner, M.; Miller, J.S. Parylene Protection Coatings for Thin Film V [TCNE]x Room Temperature Magnets. *Chem. Mater.* **2004**, *16*, 5114–5119. [CrossRef]
44. Nguyen, A.S.; Causse, N.; Musiani, M.; Orazem, M.E.; Pébère, N.; Tribollet, B.; Vivier, V. Determination of Water Uptake in Organic Coatings Deposited on 2024 Aluminium Alloy: Comparison Between Impedance Measurements and Gravimetry. *Prog. Org. Coat.* **2017**, *112*, 93–100. [CrossRef]
45. Madelat, N.; Wouters, B.; Jalilian, E.; Van Assche, G.; Hubin, A.; Terryn, H.; Hauffman, T. Differentiating between the Diffusion of Water and Ions from Aqueous Electrolytes in Organic Coatings Using an Integrated Spectro-Electrochemical Technique. *Corros. Sci.* **2023**, *212*, 110919. [CrossRef]

46. Petrunin, M.A.; Maksaeva, L.B.; Gladkikh, N.A.; Yurasova, T.A.; Maleeva, M.A.; Ignatenko, V.E. Cathodic Delamination of Polymer Coatings from Metals. Mechanism and Prevention Methods. A Review. *Int. J. Corros. Scale Inhib.* **2021**, *10*, 1–28.
47. Leidheiser, H., Jr.; Wang, W.; Igetoft, L. The Mechanism for the Cathodic Delamination of Organic Coatings from a Metal Surface. *Prog. Org. Coat.* **1983**, *11*, 19–40. [CrossRef]